PNAS RESEARCH ARTICLE | PHYSICS

Realizing one-dimensional moiré chains with strong electron localization in two-dimensional twisted bilayer WSe_2

Ya-Ning Ren[a,b], Hui-Ying Ren[a,b], Kenji Watanabe[c], Takashi Taniguchi[d], and Lin He[a,b,1]

Edited by J.C. Davis, University of Oxford, Oxford, United Kingdom; received March 19, 2024; accepted October 3, 2024

Two-dimensional (2D) moiré systems based on twisted bilayer graphene and transition metal dichalcogenides provide a promising platform to investigate emergent phenomena driven by strong electron–electron interactions in partially filled flat bands. A natural question arises: Is it possible to expand the 2D correlated moiré physics to one-dimensional (1D) that electron–electron correlation is expected to be further enhanced? This requires selectively doping of 1D moiré chain, which seems to be not within the grasp of today's technology. Therefore, an experimental demonstration of the 1D moiré chain with partially filled electronic states remains absent. Here, we show that we can introduce 1D boundaries, separating two regions with different twist angles, in twisted bilayer WSe_2 ($tWSe_2$) by using scanning tunneling microscopy (STM) and demonstrate that the electronic states of 1D moiré sites along the boundaries can be selectively filled. The strong localized charge states of correlated moiré electrons in the 1D moiré chain can be directly imaged and manipulated by combining a back-gate voltage with the STM bias voltage. Our results open the door for realizing new correlated electronic states of the 1D moiré chain in 2D systems.

flat bands | two dimensional materials | twisted bilayer | scanning tunneling microscopy

Significance

Our study expands the field of two-dimensional (2D) correlated moiré physics to one-dimensional (1D) systems. Using scanning tunneling microscopy (STM), we create 1D moiré chains in twisted bilayer WSe_2 with selectively filled electronic states. By applying a back-gate voltage and STM bias voltage, we manipulate the strong localized charge states of correlated electrons, paving the way for new correlated electronic states in 1D moiré systems.

Twisted transition metal dichalcogenide (tTMD) materials with flat bands offer an unparalleled opportunity to explore exotic strongly correlated phases in two-dimensional (2D) moiré systems (1–18). In the flat bands, the dispersion is strongly reduced, leading to enhanced electron–electron interactions for the emergence of correlated states. Usually, a back gate and/or a top gate are used to change the moiré global filling factor of the 2D system to realize the correlated states (1–18). If one can control the filling factor of selective moiré sites locally rather than globally, it will be possible to expand the 2D correlated moiré physics to one dimensional (1D) or even fractional dimensional. In previous studies, exotic correlated phenomena, such as quantum spin liquids, Tomonaga–Luttinger liquid (TLL), and Peierls-type charge density wave (CDW) have been observed in the 1D systems due to their reduced screening, enhanced quantum fluctuation, and confinement effects (19–25). Therefore, realizing 1D moiré chain may further enhance electron–electron correlation and lead to new emergent correlated electronic states that are absent in 2D moiré system. However, an experimental realization of such 1D or fractional dimensional moiré sites with partially filled electronic states has not yet been achieved.

In this work, we report a facile method to controllably introduce 1D moiré chain with strong electron localization in twisted bilayer WSe_2 ($tWSe_2$). 1D boundaries, separating two regions with different twist angles, are realized in the $tWSe_2$ by using scanning tunneling microscopy (STM) tip. Because of large local strain and lattice rotations, doping along the 1D boundary differs quite from that of the two adjacent regions, which enables us to realize partially filled electronic states only along the 1D boundary. The strongly localized correlated electrons of the local moiré sites along the 1D boundary allow us to directly image the charge states by using STM (16, 17). Moreover, our experiment indicates that the charge states of correlated moiré electrons can be manipulated by combining a back-gate voltage with the STM bias voltage.

By using micromechanical stacking technique (17, 18, 26, 27), we fabricated a high-quality $tWSe_2$ device on a hexagonal boron nitride (hBN) substrate with a graphite back gate, as schematically shown in Fig. 1*A* (*Methods* and *SI Appendix*, Fig. S1). A monolayer graphene sheet is further covered on the $tWSe_2$ device to provide a conducting layer in the STM measurements (28–30). Our experiment indicates that the topmost graphene sheet almost does not affect the electronic properties of the tTMD device, as reported previously (13, 16). Fig. 1*B* shows a large-scale STM topography image measured on the sample surface, exhibiting a quasi-1D superlattice with a period of about 100 nm, which is the superstructure of the hBN substrate. A representative zoom-in STM measurement, as shown in Fig. 1*C*, reveals a moiré superlattice morphology with an approximate

Author affiliations: [a]Center for Advanced Quantum Studies, School of Physics and Astronomy, Beijing Normal University, Beijing 100875, China; [b]Key Laboratory of Multiscale Spin Physics, Ministry of Education, Beijing 100875, China; [c]Research Center for Functional Materials, National Institute for Materials Science, Tsukuba 305-0044, Japan; and [d]International Center for Materials Nanoarchitectonics, National Institute for Materials Science, Tsukuba 305-0044, Japan

Author contributions: Y.-N.R. and L.H. designed research; Y.-N.R. performed research; K.W. and T.T. contributed high-quality hBN substrates; Y.-N.R., H.-Y.R., and L.H. analyzed data; and Y.-N.R. and L.H. wrote the paper.

The authors declare no competing interest.

This article is a PNAS Direct Submission.

[1]To whom correspondence may be addressed. Email: helin@bnu.edu.cn.

This article contains supporting information online at https://www.pnas.org/lookup/suppl/doi:10.1073/pnas.2405582121/-/DCSupplemental.

Published October 30, 2024.

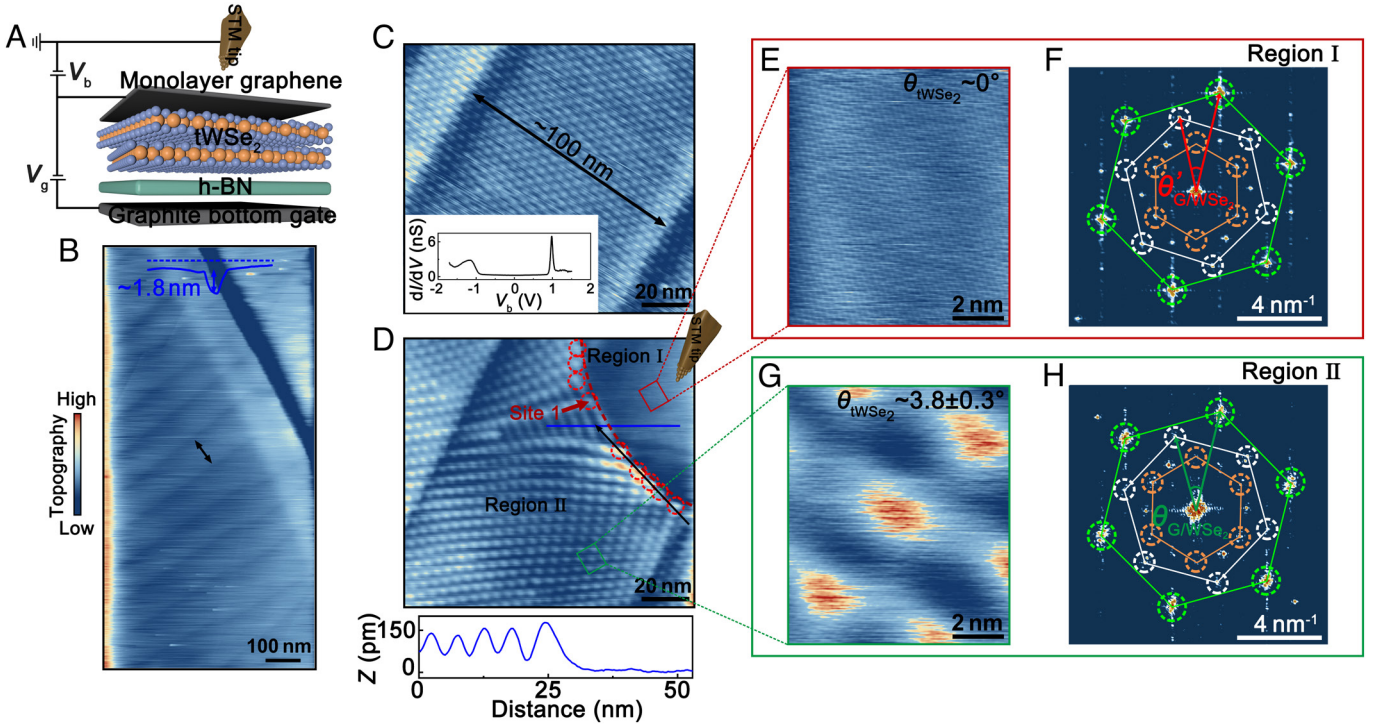

Fig. 1. In situ creating 1D moiré chain in graphene/$tWSe_2$ heterostructure. (*A*) Sketch of the heterostructure device. (*B*) A large-scale STM topography image (V_b = 1,200 mV, I = 200 pA), revealing a quasi-1D superlattice with a period ~100 nm in the hBN substrate, possibly generating by its 1D crack (see *Inset* for profile line of the 1D crack). (*C*) A zoom-in STM topographic image (V_b = −400 mV, I = 100 pA) reveals a moiré superlattice with a period ~4.4 nm. *Inset*, a d*I*/d*V* spectrum of the heterostructure. (*D*) *Top* panel: STM topographic image (V_b = −400 mV, I = 300 pA) after applying a tip pulse. The red dashed circle highlights a 1D moiré chain with different doping compared to other regions. *Bottom* panel: A height profile acquired by measuring along the blue line in the *Top* panel. (*E*–*H*) STM images and the corresponding FFT images in the region I and region II, respectively. The green, white, and orange circles show reciprocal lattices of graphene, WSe_2, and moiré lattices of the graphene/WSe_2 heterostructure, respectively.

periodicity of 4.4 nm, formed by rotating two WSe_2 layers with a twist angle $\theta \sim 4.3 \pm 0.1°$ (*SI Appendix*, Fig. S2). The 100-nm-period quasi-1D superlattice of the hBN substrate does not affect the moiré period of the $tWSe_2$, which is quite uniform in the region shown in Fig. 1*B*. Our scanning tunneling spectroscopy (STS) measurements shows a bandgap of about 2 eV in the $tWSe_2$. The moiré flat bands are observed at both the conduction band edge and valence band edge (see *Inset* of Fig. 1*C* and *SI Appendix*, Fig. S3 for spatial maps of the conduction band and valence band edges), as reported in previous studies (4, 12).

By applying an STM tip pulse, the $tWSe_2$ is locally fractured into nanoscale islands and, simultaneously, a nanoscale pit is observed around the islands in the $tWSe_2$ (*SI Appendix*, Figs. S4 and S5). The most pronounced observation in this work is that the stacking configuration between the $tWSe_2$ is changed dramatically around the pit, shown as significant changes in the moiré structure (Fig. 1*D* and *SI Appendix*, Figs. S5–S7). After the STM tip pulses, the structure of the $tWSe_2$ manifests two distinct regions separating by a sharp boundary. In region I (around the pit), the moiré pattern of the WSe_2 disappears, indicating a localized rotation between the two layers of WSe_2 to the energetically more favorable R (or H) stacking configuration (Fig. 1*E*). The profile line across the boundary, as shown in lower panel of Fig. 1*D*, excludes the increased interlayer distance between the adjacent two WSe_2 layers as the origin of the lack of moiré pattern in the region I. In region II, there is a pronounced stretching of the moiré pattern, especially near the boundary. The twist angle of the $tWSe_2$ in region II near the boundary is roughly estimated as $\theta \sim 3.8° \pm 0.3°$ according to the averaged period of the moiré pattern (see *SI Appendix*, Fig. S2 for details). It indicates that the boundary separates two regions of the WSe_2 with different twist angles, i.e., there are a large local lattice rotation and strain along the boundary. Our atomic-resolved STM measurements and the corresponding fast Fourier transform (FFT) images, as shown in Fig. 1 *E*–*H*, further reveal that there is a large lattice rotation, $\sim 3.0° \pm 0.6°$, of the topmost WSe_2 around the boundary (see *Methods* and *SI Appendix*, Fig. S2 for details). In tiny-angle twisted bilayer graphene (TBG), structure reconstruction leads to a local lattice rotation of about 1.0°, which can dramatically change electronic properties of the TBG (31–33). In our experiment, the local lattice rotation along the 1D boundary is several times larger than that in structural-reconstructed tiny-angle TBG, implying that the electronic properties of the 1D boundary could be quite different from that of its two adjacent regions.

Our STS measurement indicates that the electronic properties of the 1D boundary is changed dramatically: sharp peaks at negative energies are observed in the d*I*/d*V* spectra recorded along the boundary, as shown in Fig. 2 *A*–*C* (see *SI Appendix*, Fig. S8 for additional experimental data and similar results are obtained on different boundaries). In the tTMDs, such a phenomenon is a characteristic feature of the charging events of the local moiré sites with partially filled flat bands (16, 17). Similar charging behavior has also been observed by STM in other systems with strongly localized states (34–37). The strongly localized correlated electrons in the tTMDs enable us to directly image the charge state of the local moiré sites by using STM (16, 17). When the moiré sites on the boundary gain or lose an electron, the Coulomb potential changes, altering the electron tunneling rate between the STM tip and the sample. This, in turn, leads to the occurrence of charging events, resulting in sharp peaks in the STS spectra. As schematically shown in Fig. 2*D*, this characteristic phenomenon emerges as a consequence of partial filling of the electronic states in the valence band, where positive charges are present. Upon the application of a negative bias voltage, positive charges accumulate

at the STM tip and repel neighboring positive charges of the moiré sites through local Coulomb blockade effects. As the positive charges accumulate to a critical level, a charging process occurs at the moiré site. The charging process also can be described by tip-induced bending of the strong localized states, as illustrated subsequently.

According to our experiment, as shown in Fig. 2 *A*–*C*, the critical energy of the charging peaks sensitivity relies on relative positions of the STM tip and the moiré site. Fig. 2*C* displays representative height-dependent d*I*/d*V* spectra recorded at one of the moiré sites (see *SI Appendix*, Figs. S9 and S10 for more experimental data). As the STM tip approaches the moiré site (i.e., with decreasing junction resistances *R*), the sharp peak in the spectrum shifts toward higher energies. The underlying reason for this phenomenon stems from the fact that the charging process corresponds to the tip-induced bending of the localized states, enabling it to cross the Fermi level and resonate with it. There are three factors that affect the band bending (16, 34–41): the work function difference between the tip and $tWSe_2$ ($\Delta\Phi_{tip-tWSe_2}$), the tunneling sample bias voltage (V_b), and the back-gate voltage (V_g). Similar to previous studies (16, 38–41), the $\Delta\Phi_{tip-tWSe_2}$ elevates the moiré band (MB) beneath the tip to *p*-doping at zero sample bias voltage. A large positive bias voltage shifts the local potential distribution to deeper *p* doping and a large negative bias voltage shifts the local potential distribution to *n* doping. Consequently, the unfilled moiré band of the local moiré site beneath the STM tip crosses the Fermi level under a negative bias voltage, leading to a charging peak. With decreasing tip-sample distance vertically, the moiré band is further pushed away from the Fermi level, necessitating a higher negative bias voltage for the charging process (*SI Appendix*, Fig. S9 *D* and *E*). The energy of the moiré band can be deduced from the energy of the charging peak (*SI Appendix*, Fig. S9*C*) using the formula $e\left|V_{\text{charging}}\right| = \eta e\left|V_{\text{moiré band}}\right|$, with η as the tip lever arm. According to previous studies (42, 43), η is approximately 0.5. In the lateral direction, when the STM tip is away from a specific moiré site, the tip-induced downward band bending at the moiré site is weaker. Consequently, a higher negative energy is required to bend the moiré band to cross the Fermi level (see *SI Appendix*, Fig. S11 and Movie S1 for details). In the vicinity of the moiré site, the charging peak appears at a lower negative energy, as shown in Fig. 2 *A* and *B*. Interestingly, when the STM tip is positioned between two neighboring moiré sites, it induces multiple correlated electrons to charge the two sites in a cascading manner. As shown in Fig. 2*E*, when the STM tip is at point A, it causes the adjacent moiré sites to charge, with the electron number *n* transitioning from 0 to 1 and then to 2. During this process, a significant charging gap ($\Delta E \approx 90$ meV) appears, similar to phenomena previously observed in 2D moiré systems (16), which cannot be explained by the single-particle picture. This implies that even though the moiré sites have different on-site energies (manifested as different charging peak energies), strong correlation effects still exist. These findings provide an ideal platform for further study of strongly correlated physics governed by the 1D Hubbard model.

To further explore the charging behavior around the moiré sites along the boundary, we carry out spatially dependent d*I*/d*V* mapping. In the d*I*/d*V* maps, clear charging events were observed, characterized by prominent ring structures around the moiré sites, as shown in Fig. 3 *A* and *C* (Movies S2 and S3). As expected, the diameter of the charging rings depends sensitively on the bias voltage and the rings will even shrink to individual point at critical negative bias voltages. By comparing the d*I*/d*V* mappings with STM images, we can observe that individual charging point coincide with the moiré site positions (see *SI Appendix*, Fig. S12 for details). This indicates a strong correlation between the physical origin of the charging behavior and the moiré bands. However, our experiments reveal that the energy at which the charging peak appears depends sensitively on the moiré site, as summarized in Fig. 3 *B* and *D*. In our experiment, the subtle difference of local strain and lattice rotations on the moiré sites along the boundaries will lead to slight differences in the filling between different moiré sites, resulting in

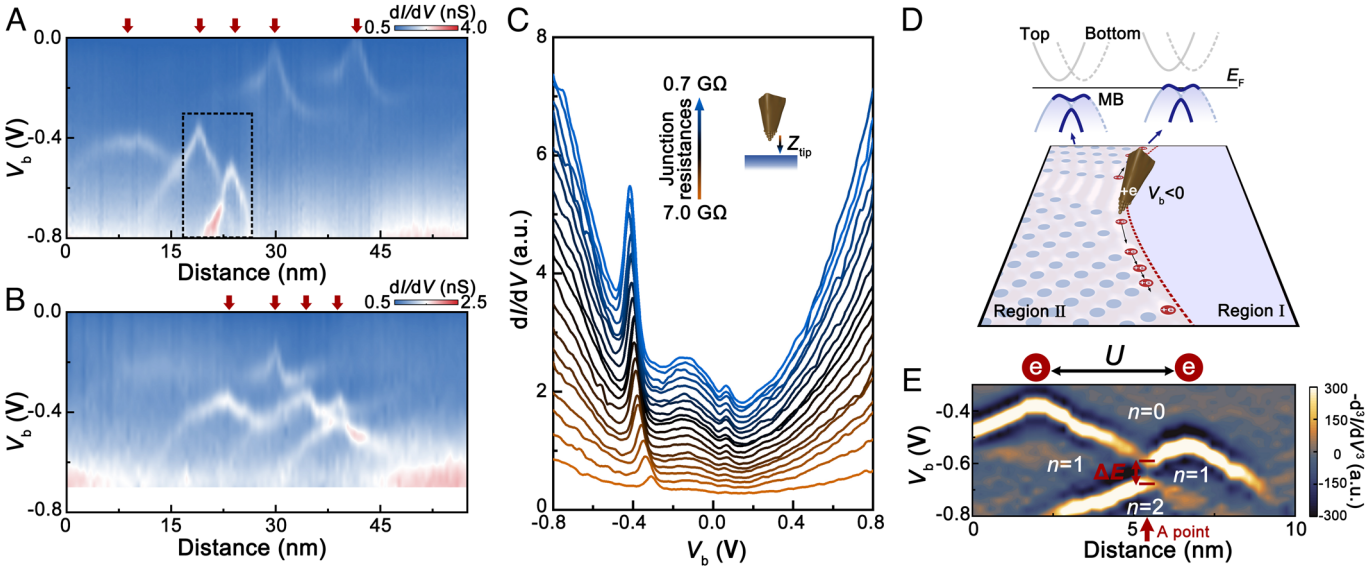

Fig. 2. Local charging effect of moiré sites along the 1D boundary. (*A* and *B*), The d*I*/d*V* spectroscopic maps versus the spatial position along black solid arrows (*A*) in Fig. 1*D* and (*B*) in *SI Appendix*, Fig. S7, respectively. (*C*) The d*I*/d*V* spectra measured at different tip-sample distances Z_{tip}. The curves are shifted vertically by 0.05 each for clarity. The tip height decreases as the preset tunneling current (*I*) is changed from 0.1 nA to 1 nA, while maintaining a fixed bias voltage of $V_b = -0.7$ V. The junction resistances are derived from $R = V_b/I$. (*D*) Sketch of the tip-induced charging effect at the moiré sites along the 1D boundary. When the positive charges of the tip accumulate to a critical level, a charging process occurs at the moiré site, resulting in the switch of charge-neutral state V^0 to negative state V^-. (*E*) A zoom-in d*I*/d*V* spectroscopic map of black dashed frame in panel *A*, which passes through two moiré sites. To selectively characterize the charging peak, we take the negative of the second derivative $-(\mathrm{d}I/\mathrm{d}V)'' = -\mathrm{d}^3I/\mathrm{d}V^3$ of each d*I*/d*V* spectrum. The charging peak demonstrates charge events corresponding to total electron number *n* transitioning from 0 to 1, and then to 2, with increasing negative bias voltage. At point A, two charging events occur at different V_b values, with a charging gap of $\Delta E \approx 90$ mV, which cannot be explained by the single-particle picture, indicating the presence of electron correlations in this system.

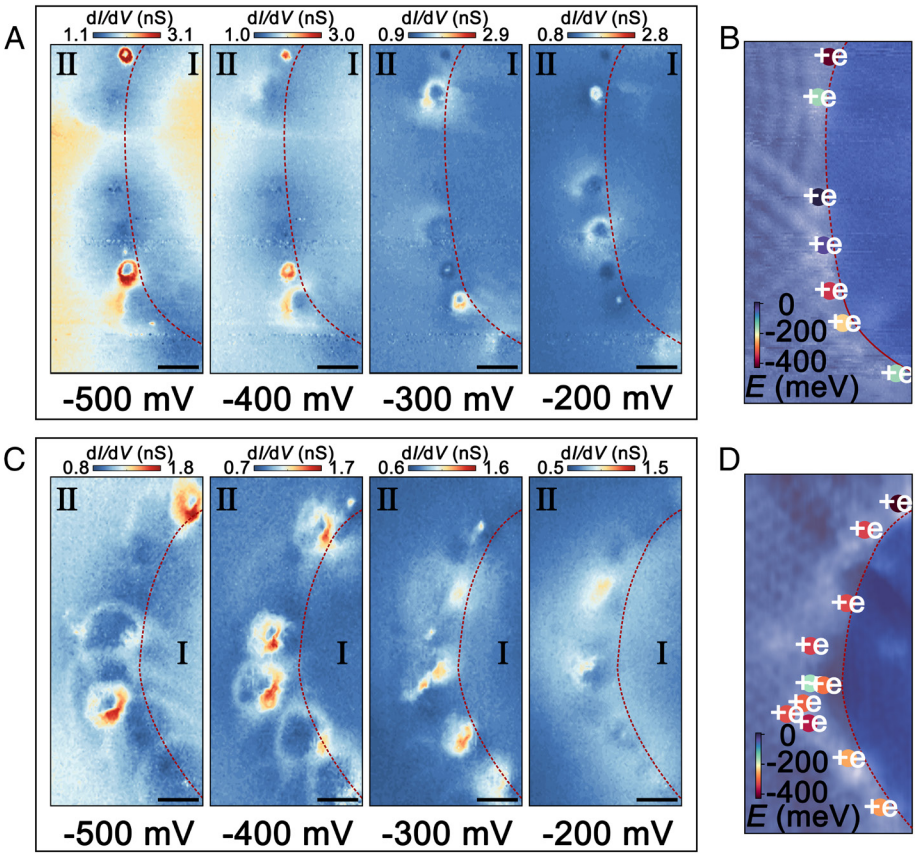

Fig. 3. Evolution of moiré charging rings with changing V_b. (*A*) Spatial-dependent d*I*/d*V* mappings on the boundary region. The scale bar is 10 nm. (*B*) A statistical summary showing the critical energy at which the charging peak appears for each moiré site in panel *A*. The different colors represent different energy values. (*C*) Spatial-dependent d*I*/d*V* mappings on another boundary region. The scale bar is 10 nm. (*D*) A statistical summary showing the critical energy at which the charging peak appears for each moiré site in panel *C*. The different colors represent different energy values.

differences in the energy required for the moiré band to bend to the Fermi level, i.e., the different energies at which the charging peak appears. Previous studies have demonstrated explicitly that the tTMD moiré heterostructures provide a platform for simulating strongly correlated physics in the 2D extended Hubbard model (1–4, 15), and the different energies at which the charging peak appear are observed in the STM measurements and they are described by different Hubbard on-site energies (16). In the near future, more efforts are needed to reduce the difference of the Hubbard on-site energies along the 1D moiré chain to increase the correlations among the moiré sites.

To further investigate the influence of filling on the charging effect, we applied a back gate to control the carrier density. Fig. 4 *A* and *B* show two representative gate-dependent d*I*/d*V* spectra obtained at two different sites, labeled as sites 1 and 2 respectively (see *SI Appendix*, Figs. S13 and S14 for details and see *SI Appendix*, Fig. S15 for more experimental results). The site 1 is near the center of one moiré site (as shown in Fig. 1*D*), therefore, we only detect the charging peak of one moiré site. The site 2 is located in a densely packed moiré region, allowing us to probe the charging behavior of three neighboring moiré sites (as shown in *SI Appendix*, Fig. S7). Obviously, in both cases, the energies of the charging peaks depend sensitively on the back-gate voltage. With increasing the back-gate voltage from −20 V to 16 V, the moiré band is tuned from positive energy to approach the Fermi level. Therefore, a smaller negative bias voltage on the tip is enough to bend it to the Fermi level for the charging process, as observed in Fig. 4 *A* and *B*. The opposite trend of this movement compared to normal states further confirms the nature of these peaks as charging peaks, fully confirming that the charging behavior is determined by the filling of the moiré band. Our d*I*/d*V* mappings at a back-gate voltage of 15 V, as summarized in Fig. 4 *C*–*F*, further demonstrate the above result (Movie S4). There are two distinct charging behaviors of different moiré sites. In case 1, the diameter of the charging ring for some moiré sites decreases by further increasing the negative bias voltages. As an example, the charging ring observed at −77 mV is larger than that observed at −135 mV (Fig. 4*C*). In case 2, the opposite behavior is observed and the diameter of the charging ring for the other moiré sites increases by further increasing the negative bias voltages, as observed in Fig. 4*E*. All these phenomena can be understood self-consistently with the moiré band filling picture. In the case 1, the moiré band for the moiré sites is completely filled in the absence of tip-induced bending. Then, the tip-induced band bending allows us to detect the charging peaks at a small bias voltage. As the negative bias voltage increases, the band gradually bends downward, reducing the degree of upward band bending and causing the diameter of the charging ring to decrease until it disappears (Fig. 4*D*). In the case 2, the moiré band is slightly above the Fermi level in the absence of tip-induced bending. As the negative bias voltage increases, the moiré band of these moiré sites bends toward the Fermi level, leading to the appearance of charging peaks. With further increase of the negative bias voltage, the degree of band bending increases, resulting in an increase in the diameter of the charging ring (Fig. 4*F*). The emergence of two distinct charging behaviors of different moiré sites further confirms the different fillings of the moiré sites along the boundary. The different fillings, i.e., the subtle energy difference between the moiré band and the Fermi level, in different moiré sites in turn results in different band bending effects under various bias voltage and back-gate voltage.

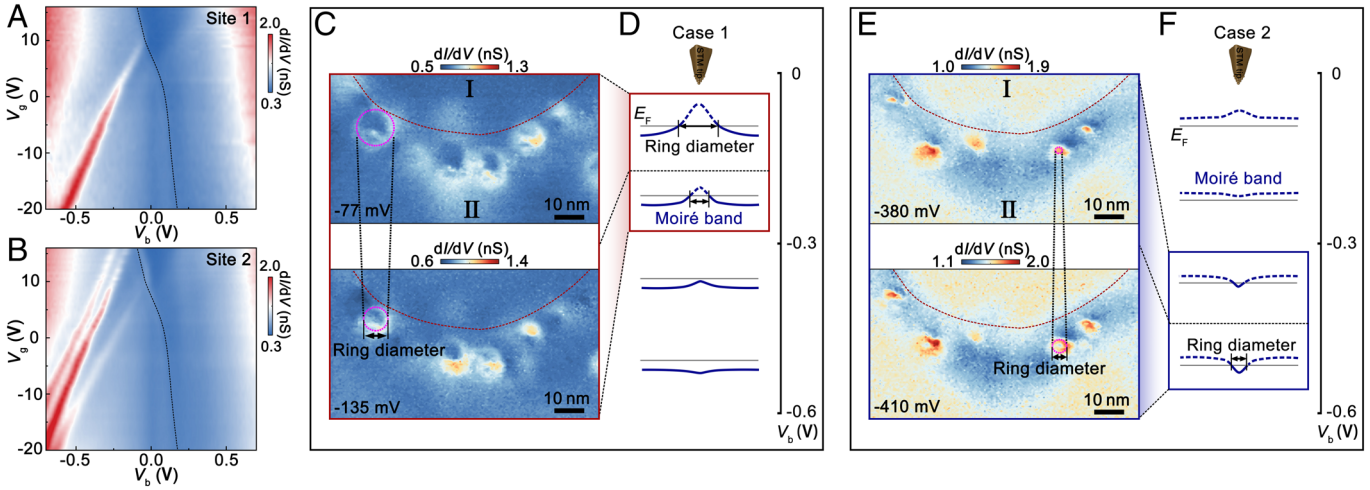

Fig. 4. The impact of electron fillings on the charging effect of moiré sites. (*A* and *B*), Gate-dependent d*I*/d*V* spectra measured at two different moiré sites. Site 1 is labeled in Fig. 1*D*, while site 2 is labeled in *SI Appendix*, Fig. S7. The black dashed lines indicate the energy of the graphene Dirac point far from the 1D moiré sites (~ 30 nm) at various back-gate voltages. (*C*) Spatially dependent d*I*/d*V* mappings at different energies with V_g = 15 V. (*D*) Schematic diagram of the band filling as a function of bias voltage for case 1, where the diameter of the charging ring observed at high negative energy is smaller than that observed at low negative energy. (*E*) Spatially dependent d*I*/d*V* mappings at different energies with V_g = 15 V. (*F*) Schematic diagram of the band filling as a function of bias voltage for case 2, where the diameter of the charging ring observed at high negative energy is larger than that observed at low negative energy.

In conclusion, we present a facile and general approach to implement 1D moiré chains with partially filled moiré bands within 2D TMD systems. This methodology establishes a pioneering moiré superlattice platform for simulation of strongly correlated physics that is governed by the 1D Hubbard model. The reported results pave the way for expanding the 2D correlated moiré physics to 1D or even fractional dimensional, offering uncommon opportunities for studying and comprehending the intricacies of strongly correlated physics.

Methods

Sample Fabrication. The graphene/tWSe_2 heterostructure was fabricated using the micromechanical stacking technique (18, 27) based on the transfer platform from Shanghai Onway Technology Co., Ltd. By utilizing a polydimethylsiloxane (PDMS) film stamp, the process of sequentially picking up all exfoliated 2D material flakes on the PDMS film is performed in the following order: the bottom hBN layer, the first layer of WSe_2, the second layer of WSe_2, and then monolayer graphene. The two WSe_2 layer achieves relative rotation of approximately 4° based on straight edge alignment. Subsequently, the entire heterostructure is flipped using another PDMS film, and the original PDMS film is removed. The heterostructure is then placed on a SiO_2/Si substrate, which is prepatterned with few-layered graphene or gold electrodes. Finally, electrical contact is established by connecting the electrodes to the sample surface using a graphite thin film.

STM Measurements. STM/STS measurements were performed in low-temperature (77 K) and ultrahigh-vacuum (~10^{-10} Torr) scanning probe microscopes (USM-1400) from UNISOKU. The tips were obtained by chemical etching from a tungsten wire. The differential conductance (d*I*/d*V*) measurements were taken by a standard lock-in technique with an ac bias modulation of 5 mV and 793 Hz signal added to the tunneling bias.

The Relative Lattice Rotation Angle of WSe_2 on Both Sides of the 1D Moiré Chain. The angle difference in the WSe_2 lattice on both sides of the 1D moiré chain can be corroborated by two methods.

Method 1. Comparing the twist angles of tWSe_2 on both sides of the moiré chain. In region I, there is no tWSe_2 moiré pattern (as shown in *SI Appendix*, Fig. S2*G*), indicating that the twist angle tends towards 0° at this location. In region II, the twist angle between the two WSe_2 layers (θ_{tWSe_2}) is approximately 3.8 ± 0. 3°, based on the measured periods L_n, (n = 1, 2, 3) according to $L = a/[2\sin(\theta/2)]$, where $a = 0.328$ nm is the WSe_2 lattice constant. The measured periods in three directions are L_1 = 4.40 nm, L_2 = 5.10 nm, and L_3 = 5.25 nm (as shown in *SI Appendix*, Fig. S2*E*). Therefore, the relative lattice rotation of WSe_2 on either side of the moiré chain is ~3.8 ± 0.3°.

Method 2. Comparing the twist angles between graphene and WSe_2 on both sides of the moiré chain. We can analyze the twist angle θ_{G/WSe_2} between graphene and WSe_2 from the FFT, as depicted in *SI Appendix*, Fig. S2 *F*, *H*, and *I*. The θ_{G/WSe_2} is (27.16 ± 0.60)° in region I, and approximately (30.12 ± 0.23)° in region II. Subtracting these angles yields a lattice rotation angle of WSe_2, $\Delta\theta_{WSe_2}$, of ~(3.0 ± 0.6)° between the two regions, which is consistent with the results obtained using *Method 1*.

Data, Materials, and Software Availability. All study data are included in the article and/or supporting information.

ACKNOWLEDGMENTS. This work was supported by the National Key R and D Program of China (Grant Nos. 2021YFA1401900, 2021YFA1400100), National Natural Science Foundation of China (Grant Nos. 12141401, 12425405, and 12404198), "the Fundamental Research Funds for the Central Universities" (Grant No. 310400209521), the China National Postdoctoral Program for Innovative Talents (Grant No. BX20240040), and the China Postdoctoral Science Foundation (2023M740296). The devices were fabricated using the transfer platform from Shanghai Onway Technology Co., Ltd.

1. Y. Tang *et al.*, Simulation of Hubbard model physics in WSe_2/WS_2 moiré superlattices. *Nature* **579**, 353–358 (2020).
2. E. C. Regan *et al.*, Mott and generalized Wigner crystal states in WSe_2/WS_2 moiré superlattices. *Nature* **579**, 359–363 (2020).
3. L. Wang *et al.*, Correlated electronic phases in twisted bilayer transition metal dichalcogenides. *Nat. Mater.* **19**, 861–866 (2020).
4. Y. Xu *et al.*, A tunable bilayer Hubbard model in twisted WSe_2. *Nat. Nanotech.* **17**, 934–939 (2022).
5. K. L. Seyler *et al.*, Signatures of moiré-trapped valley excitons in $MoSe_2/WSe_2$ heterobilayers. *Nature* **567**, 66–70 (2019).
6. K. Tran *et al.*, Evidence for moiré excitons in van der Waals heterostructures. *Nature* **567**, 71–75 (2019).
7. C. Jin *et al.*, Observation of moiré excitons in WSe_2/WS_2 heterostructure superlattices. *Nature* **567**, 76–80 (2019).
8. E. Liu *et al.*, Signatures of moiré trions in $WSe_2/MoSe_2$ heterobilayers. *Nature* **594**, 46–50 (2021).
9. L. Balents, C. R. Dean, D. K. Efetov, A. F. Young, Superconductivity and strong correlations in moiré flat bands. *Nat. Phys.* **16**, 725–733 (2020).
10. E. Y. Andrei, A. H. MacDonald, Graphene bilayers with a twist. *Nat. Mater.* **19**, 1265–1275 (2020).
11. Y.-N. Ren, Y. Zhang, Y.-W. Liu, L. He, Twistronics in graphene-based van der Waals structures. *Chin. Phys. B* **29**, 117303 (2020).
12. Z. Zhang *et al.*, Flat bands in twisted bilayer transition metal dichalcogenides. *Nat. Phys.* **16**, 1093–1096 (2020).

13. H. Li *et al.*, Imaging moiré flat bands in three-dimensional reconstructed WSe_2/WS_2 superlattices. *Nat. Mater.* **20**, 945–950 (2021).
14. E. Li *et al.*, Lattice reconstruction induced multiple ultra-flat bands in twisted bilayer Wse_2. *Nat. Commun.* **12**, 5601 (2021).
15. F. Wu, T. Lovorn, E. Tutuc, A. H. MacDonald, Hubbard model physics in transition metal dichalcogenide moiré bands. *Phys. Rev. Lett.* **121**, 026402 (2018).
16. H. Li *et al.*, Imaging local discharge cascades for correlated electrons in WS_2/Wse_2 moiré superlattices. *Nat. Phys.* **17**, 1114–1119 (2021).
17. H. Li *et al.*, Imaging two-dimensional generalized Wigner crystals. *Nature* **597**, 650–654 (2021).
18. D. Pei *et al.*, Observation of Γ-Valley moiré bands and emergent hexagonal lattice in twisted transition metal dichalcogenides. *Phys. Rev. X* **12**, 021065 (2022).
19. P. W. Anderson, Resonating valence bonds: A new kind of insulator? *Mater. Res. Bull.* **8**, 153–160 (1973).
20. B. J. Kim *et al.*, Distinct spinon and holon dispersions in photoemission spectral functions from one-dimensional $SrCuO_2$. *Nat. Phys.* **2**, 397–401 (2006).
21. B. Lake, D. A. Tennant, C. D. Frost, S. E. Nagler, Quantum criticality and universal scaling of a quantum antiferromagnet. *Nat. Mater.* **4**, 329–334 (2005).
22. C. Broholm *et al.*, Quantum spin liquids. *Science* **367**, eaay0668 (2020).
23. T. Zhu *et al.*, Imaging gate-tunable Tomonaga-Luttinger liquids in 1H-$MoSe_2$ mirror twin boundaries. *Nat. Mater.* **21**, 748–753 (2022).
24. W. Jolie *et al.*, Tomonaga-Luttinger liquid in a box: Electrons confined within MoS_2 mirror-twin boundaries. *Phys. Rev. X* **9**, 011055 (2019).
25. L. Wang *et al.*, Direct observation of one-dimensional Peierls-type charge density wave in twin boundaries of monolayer $MoTe_2$. *ACS Nano* **14**, 8299–8306 (2020).
26. Q. Zheng *et al.*, Tunable sample-wide electronic Kagome lattice in low-angle twisted bilayer graphene. *Phys. Rev. Lett.* **129**, 076803 (2022).
27. C.-Y. Hao *et al.*, Creating a custom-designed moiré magnifying glass to probe local atomic lattice rotations in twisted bilayer graphene. *Phys. Rev. B* **108**, 125429 (2023).
28. H.-Y. Ren *et al.*, Electron–electron interaction and correlation–induced two density waves with different Fermi velocities in graphene quantum dots. *Phys. Rev. B* **108**, L081408 (2023).
29. Q. Zheng *et al.*, Molecular collapse states in graphene/WSe_2 heterostructure quantum dots. *Phys. Rev. Lett.* **130**, 076202 (2023).
30. Q. Zheng, Y. Zhuang, Q.-F. Sun, L. He, Coexistence of electron whispering gallery modes and atomic collapse states in graphene/WSe2 heterostructure quantum dots. *Nat. Commun.* **13**, 1597 (2022).
31. H. Yoo *et al.*, Atomic and electronic reconstruction at the van der Waals interface in twisted bilayer graphene. *Nat. Mater.* **18**, 448–453 (2019).
32. N. P. Kazmierczak *et al.*, Strain fields in twisted bilayer graphene. *Nat. Mater.* **20**, 956–963 (2021).
33. Y.-N. Ren *et al.*, Real-space mapping of local sub-degree lattice rotations in twisted bilayer graphene magnified by moiré superlattices. *Nano Lett.* **23**, 1836 (2023).
34. N. A. Pradhan, N. Liu, C. Silien, W. Ho, Atomic scale conductance induced by single impurity charging. *Phys. Rev. Lett.* **94**, 076801 (2005).
35. K. Teichmann *et al.*, Controlled charge switching on a single donor with a scanning tunneling microscope. *Phys. Rev. Lett.* **101**, 076103 (2008).
36. V. W. Brar *et al.*, Gate-controlled ionization and screening of cobalt adatoms on a graphene surface. *Nat. Phys.* **7**, 43–47 (2011).
37. D. Wong *et al.*, Characterization and manipulation of individual defects in insulating hexagonal boron nitride using scanning tunnelling microscopy. *Nat. Nanotechnol.* **10**, 949 (2015).
38. Y. Zhao *et al.*, Creating and probing electron whispering-gallery modes in graphene. *Science* **348**, 672–675 (2015).
39. Y.-N. Ren *et al.*, Spatial and magnetic confinement of massless Dirac fermions. *Phys. Rev. B* **104**, L161408 (2021).
40. Y.-N. Ren, Q. Cheng, Q.-F. Sun, L. He, Realizing valley-polarized energy spectra in bilayer graphene quantum dots via continuously tunable Berry phases. *Phys. Rev. Lett.* **128**, 206805 (2022).
41. S.-Y. Li, Y. Su, Y.-N. Ren, L. He, Valley polarization and inversion in strained graphene via pseudo-Landau levels, valley splitting of real Landau levels, and confined states. *Phys. Rev. Lett.* **124**, 106802 (2020).
42. N. M. Freitag *et al.*, Electrostatically confined monolayer graphene quantum dots with orbital and valley splittings. *Nano Lett.* **16**, 5798–5805 (2016).
43. N. M. Freitag *et al.*, Large tunable valley splitting in edge-free graphene quantum dots on boron nitride. *Nat. Nanotech.* **13**, 392–397 (2018).